Bollettino di Geofisica Teorica ed Applicata Vol. 59, n. 2, pp. 161-178; June 2018
DOI 10.4430/bgta0233

Application of the tilt angle of the balanced total horizontal derivative filter for the interpretation of potential field data

A. Eshaghzadeh[1] and A. Hajian[2]

[1] *Institute of Geophysics, University of Tehran, Iran*

[2] *Department of Physics, Islamic Azad University, Najafabad, Iran*

(Received: 31 December 2017; accepted: 12 May 2018)

ABSTRACT Various filtering approaches are used to determine the approximate border of potential field sources buried at different depths. We have developed a new edge detector method to delineate the causative mass limit of potential field anomalies titled "the tilt angle of the balanced total horizontal derivative" (*TBHD*). In this paper, we suggest using *TBHDs* in the Euler method instead of potential field derivatives, as prior information about the structural index is not necessary. We have named this method *TBHD*-EUL. The *TBHD* and *TBHD*-EUL methods are examined on synthetic gravity and magnetic anomalies. The estimated results show that both methods can accurately indicate the anomalies edges location for noise-free data, and also attain acceptable results for noise-corrupted data. We applied the *TBHD* and *TBHD*-EUL methods to real gravity data from Iran. The horizontal location of the solutions obtained by the *TBHD*-EUL method lies on the anomalies boundary which the *TBHD* filter has detected. The solutions from *TBHD*-EUL are compared with results from the standard Euler deconvolution method. The depth values of the solutions estimated by the *TBHD*-EUL method show a more limited variation range and better stability of the responses than the solutions of the standard Euler deconvolution method.

Key words: potential fields, tilt angle of the balanced total horizontal derivative (*TBHD*), Euler deconvolution, Iran, *TBHD*-EUL method.

1. Introduction

Gravity and magnetic operations are widely carried out for mineral resource explorations and geological studies. An important objective in interpreting potential field data is to determine the causative source parameters, such as the locations of boundaries and depths.

Enhancement methods are useful devices that have frequently been used to facilitate qualitative interpretations of the gravity and magnetic anomalies in terms of underground causative masses.

Vertical and horizontal derivatives have been used for many years to delineate the edges of the geological structures and buried source bodies in gravity and magnetic field maps (Evjen, 1936; Cordell, 1979; Cordell and Grauch, 1985; Blakely and Simpson, 1986; Hood and Teskey, 1989; Roest *et al.*, 1992; Fedi and Florio, 2001). Many commonly employed filters to amplify details and causative source edges in potential field maps are based on combinations of the horizontal

and vertical derivatives of the potential data, i.e. the tilt angle [TDR: Miller and Singh (1994)], the Theta map (Wijns *et al.*, 2005), the total horizontal derivative of the tilt angle [*THDR*: Verduzco *et al.* (2004)], the horizontal tilt angle [TDX: Cooper and Cowan (2006)], the balanced analytic signal (Cooper, 2009), the terracing method (Cooper and Cowan, 2009), the wavelet analysis (Alp *et al.*, 2011), the normalized horizontal derivative (Ma and Li, 2012), the tilt angle of the horizontal gradient (Ferreira *et al.*, 2013). Yuan *et al.* (2014) proposed three improved methods to balance the large eigenvalue of the structure tensor since the large eigenvalue outlines the edges of causative bodies. Eshaghzadeh and Kalantari (2017) have applied the Canny edge detection algorithm to interpret potential fields and they were able to determine the anomalies border successfully. Görgün and Albora (2017) applied the steerable filter technique to the gravity anomaly map of Biga Peninsula.

A range of semiautomatic interpretation techniques have been extended to determine the depths of the causative mass or specify the boundaries and depths of the anomaly sources simultaneously. Techniques based on the first and second order derivatives of potential fields, such as Euler deconvolution (Thompson, 1982; Reid *et al.*, 1990) and proposed methods by Blakely (1995), Nabighian *et al.* (2005) and Salem *et al.* (2005, 2008), are being used more broadly and can be applied to obtain both a border location and a depth for the anomaly sources. Moreover, inversion methods (Abdelrahman, 1990; Abdelrahman and El-Araby, 1993; Abdelrahman *et al.*, 2001; Essa, 2007), SPI method (Thurston and Smith, 1997) and tilt-distance-depth method (Eshaghzadeh, 2017), can be used to evaluate the depth for anomaly generating mass.

A well-known and popular approach of the techniques abovementioned is the Euler deconvolution method. The inversion of Euler deconvolution requires information about the nature (structural index) of the source relative to the mass shape, but the structural index is non-unique and hard to estimate for an unknown region. To compute the causative source locations without using the information about structural index, several extended Euler deconvolution methods have been introduced (Mushayandebvu *et al.*, 2001; Hsu, 2002; Gerovska and Arauzo-Bravo, 2003; Salem and Ravat, 2003; FitzGerald *et al.*, 2004; Salem *et al.*, 2008; Ma, 2013, 2014; Ma *et al.*, 2013).

In this paper, we first present the new method "the tilt angle of the balanced total horizontal derivative" (*TBHD*) that serves as an edge detector filter. We go on to develop the Euler deconvolution method by using first-order horizontal and vertical derivatives of the *TBHD* instead of potential field derivatives. In this study, this approach is introduced as *TBHD*-EUL.

2. Improved edge detection method

The total horizontal derivative (*THDR*) is a prevalent edge-detection filter, as given by (Cooper and Cowan, 2008):

$$THDR = \sqrt{\left(\left(\frac{\partial F}{\partial x}\right)^2 + \left(\frac{\partial F}{\partial y}\right)^2\right)} \qquad (1)$$

where F is the gravity or magnetic anomaly. Miller and Singh (1994) introduced the tilt angle, namely the ratio of the vertical derivative to the total horizontal derivative, which is defined as:

$$TA = \tan^{-1}\left(\frac{\partial F / \partial z}{THDR}\right). \tag{2}$$

If the density contrast of the causative mass is positive, the tilt angle value over the source is positive, it is zero or close to zero over or near the edge where the vertical derivative is zero and the horizontal derivative is a maximum. The tilt angle value is negative outside the source limits. The tilt angle has a range of -90° to $+90^\circ$ and is much easier to interpret than the analytic signal phase angle (Cooper and Cowan, 2006). Cooper (2009) proposed a new method based on balancing the derivatives of potential field data using its orthogonal Hilbert transforms titled "balanced total horizontal derivative" (*THDRB*), defined as:

$$THDRB = \frac{THDR}{k + \sqrt{((H_x(THDR))^2 + (H_y(THDR))^2 + THDR^2)}} \tag{3}$$

where H_x and H_y are the Hilbert transforms of the total horizontal derivative in the x and y directions, respectively; the constant k controls the amount of amplitude balancing and *THDR* is computed by Eq. 1.

This paper presents a novel edge detection technique that is based on the intensification of the *THDRB* of potential field anomalies using the tilt angle filter. It can be termed the tilt angle of the balanced total horizontal derivative (*TBHD*) method, and may be expressed as:

$$TBHD = \tan^{-1}\left(\frac{\frac{\partial THDRB}{\partial z}}{\sqrt{\left(\frac{\partial THDRB}{\partial x}\right)^2 + \left(\frac{\partial THDRB}{\partial y}\right)^2}}\right) \tag{4}$$

In this study, the efficiency of the *TBHD* is considered for a synthetic gravity and magnetic data set. The *TBHD* transform range is from $-\pi/2$ to $+\pi/2$. The maximum amplitude of the *TBHD* always enhances the anomaly edges of any orientation.

3. Edge determination for synthetic models

In this part, the performance of the *THDRB* and *TBHD* filters are evaluated and compared for gravity and magnetic fields data according to two discrete theoretical models. Fig. 1 displays the gravity field data set of the synthetic model consisting of two separate rectangular blocks, outlined in black, at different depths in a 200×200 m^2 grid. The lower rectangular prism size on the left of grid is 40×100×50 m^3 and the upper rectangular prism size on the right of grid is 60×60×50 m^3 as located at a depth of 10 and 5 m, respectively. The assumed density contrast for both rectangular prisms is 1 g/cm^3 (Table 1).

Fig. 2 shows the output maps as a result of employing the *THDRB* and *TBHD* transform to the gravity data in Fig. 1. *THDRB* map was produced using $k = 1$ in Eq. 3. The *THDRB*

Table 1 - Details of the gravity and magnetic synthetic models.

Parameters		Length (m)	Width (m)	Height (m)	Depth to top (m)	Density contrast (gr/cm^3)	Magnetization intensity (A/m)
Gravity model	left	100	40	50	10	1	---
	right	60	60	50	5	1	---
Magnetic model		100	100	50	20	---	5

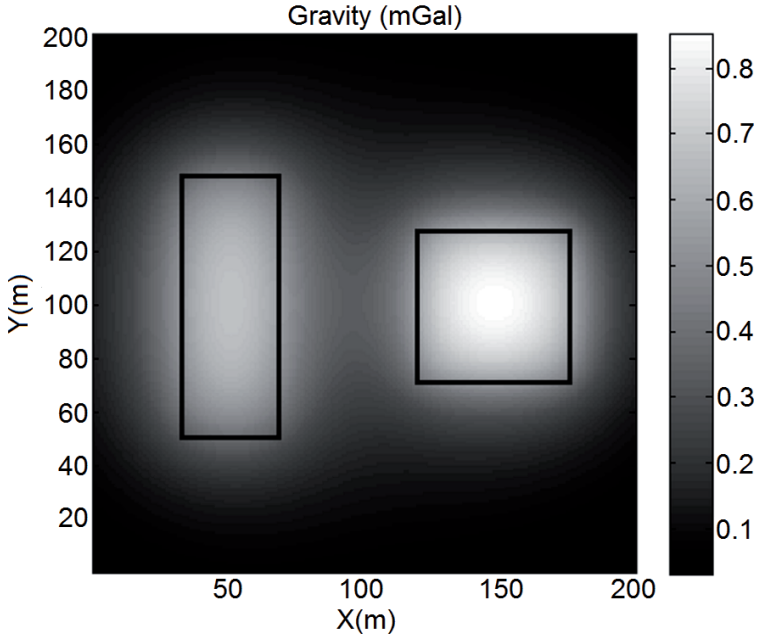

Fig. 1 - The synthetic gravity field of two separate rectangular blocks, outlined in black, at different depths.

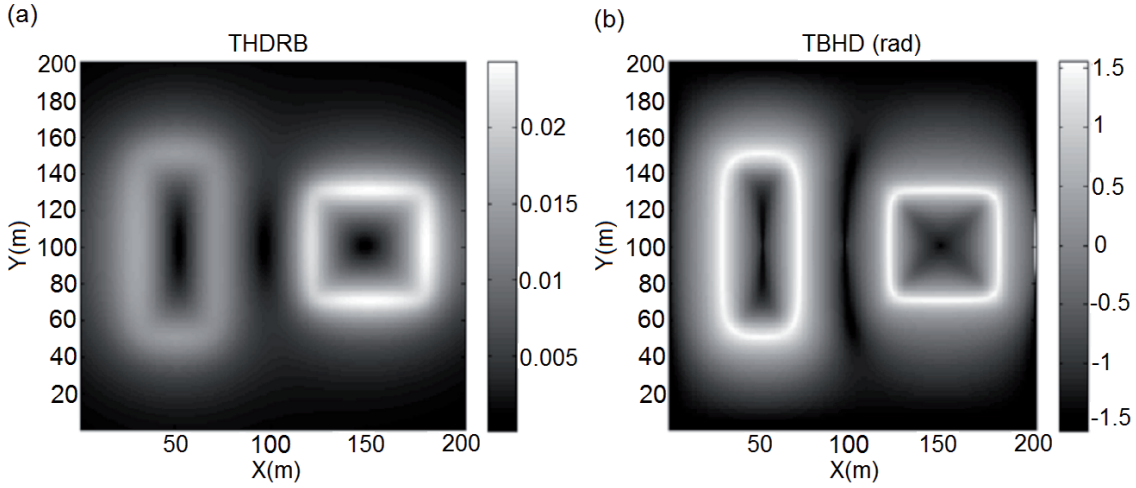

Fig. 2 - Output maps as a result of applying the *THDRB* (a) and *TBHD* (b) filters to the gravity data in Fig. 1.

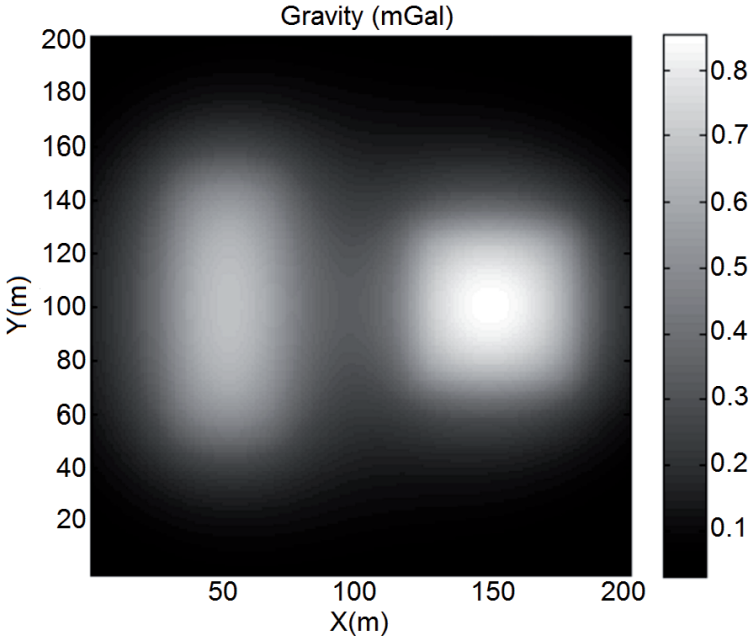

Fig. 3 - The gravity response in Fig. 1 has been corrupted by a random noise with a mean of 0.05 mGal and standard deviation of 0.01 mGal.

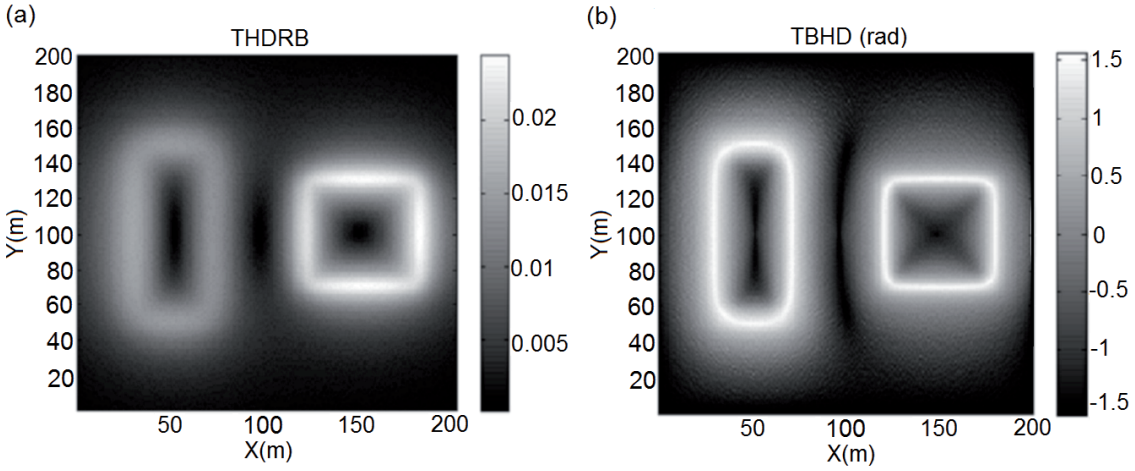

Fig. 4 - Output maps as a result of applying the *THDRB* (a) and *TBHD* (b) filters to the noisy gravity data in Fig. 3.

(Fig. 2a) locates the prism edges but its maximum amplitude values are diffuse around the edges and the borders are blurred. The response from the deeper source is also relatively vague. Thus, the filtered data decreases in amplitude as depth increases. In comparison with the *THDRB*, in the *TBHD* map (Fig. 2b) the edges of the source bodies at different depths are precisely delineated by a narrow line of the maximal transformed signals.

The effect of random error is investigated by adding a matrix of the random values with a mean of 0.05 mGal and standard deviation of 0.01 mGal to the gravity response of the synthetic model in Fig. 1 (Fig. 3). The interpretation for the converted noisy anomalies as a result of the *THDRB* and *TBHD* filters application (Fig. 4), is similar to the free noise data set. Because the *TBHD* included the horizontal and vertical derivatives of the *THDRB*, it is sensitive to noise.

Although the *THDRB* is less sensitive to noise than the *TBHD* method, the maximum values are more diffuse around the edges and the strength of the transformed signal is gradually weakened with depth.

Fig. 5 represents the theoretical magnetic field due to a rectangle prism whose size is $100\times100\times50$ m^3 at a depth of 20 m map in balck on a 200×200 m^2 grid (Table 1). The assumed declination and inclination angles for both the geomagnetic field and model magnetization are zero and 90 degrees, respectively (reduced to pole). The magnetization intensity is considered 5 A/m. Note that boundaries conditions relative to geological structures in magnetic data will only be correctly located if the data has formerly been reduced to the pole.

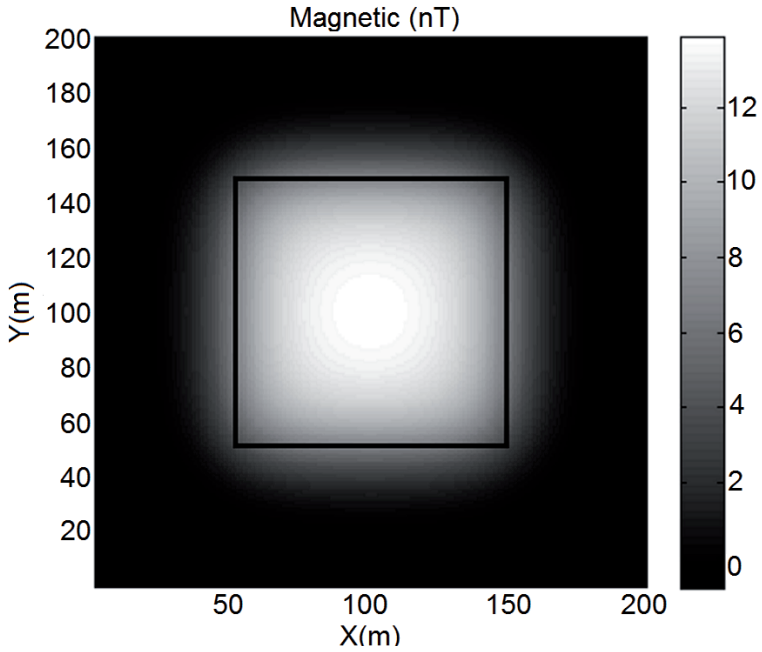

Fig. 5 - The theoretical magnetic field due to a rectangle prism at a depth of 20 m (top) where outlined in black.

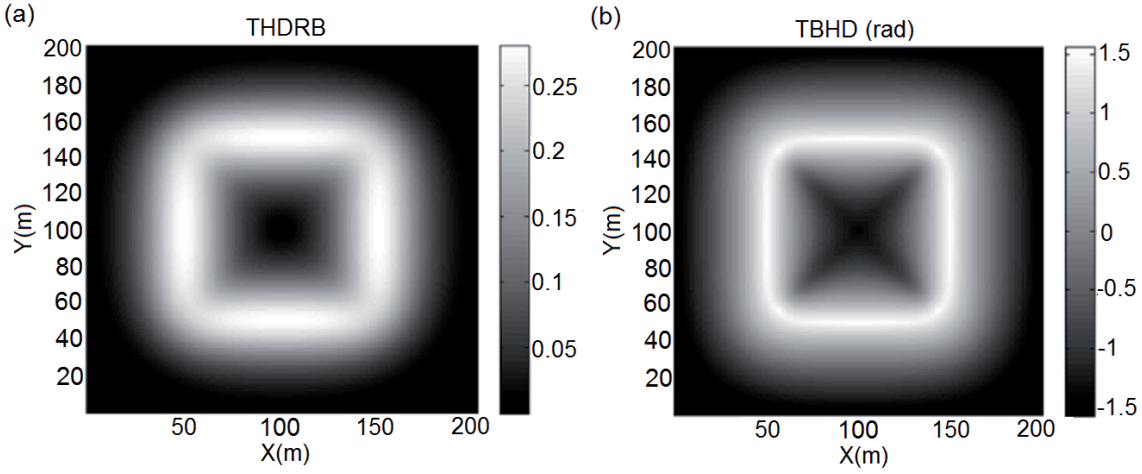

Fig. 6 - Output maps as a result of applying the *THDRB* (a) and *TBHD* (b) filters to the magnetic data in Fig. 5.

The maximum values of the tilt angle of the *TBHD* enhance the location of the body edges, to form a sharp and delicate peak; instead the *THDRB* filter provides signals whose amplitude are bigger, spread above and around the edges, as shown in Fig. 6.

Fig. 7 shows the data in Fig. 5 that have been corrupted by a series of random noise with a mean of 0.5 nT and standard deviation of 0.1 nT, in order to evaluate the influence of eventual noise existence in the data set. The *TBHD* (Fig. 8b) has an improved performance in the presence of noise, compared with the *THDRB* (Fig. 8a). Though the transformed map of the noise corrupted magnetic data by the *TBHD* method has been covered with the noise points, but shows the acceptable results as an edge detector.

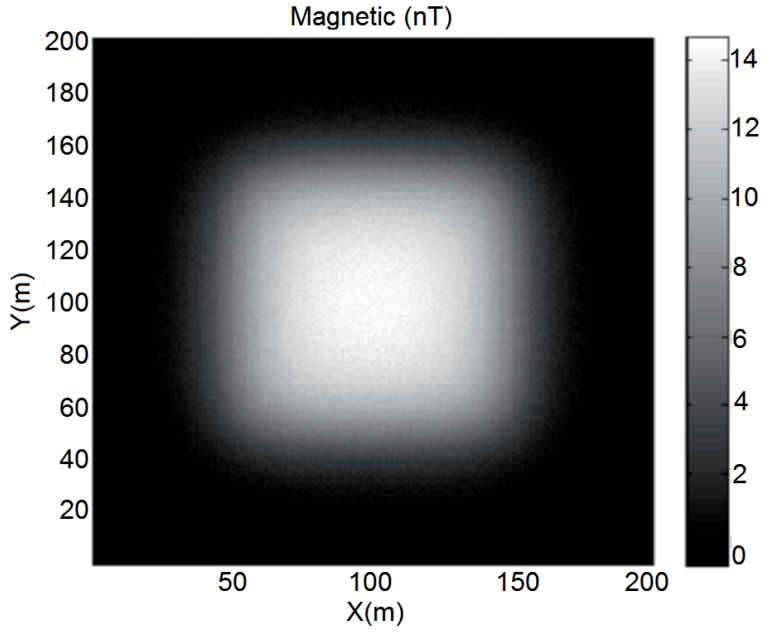

Fig. 7 - The magnetic response in Fig. 5 as corrupted by a random noise with a mean of 0.5 nT and standard deviation of 0.1 nT.

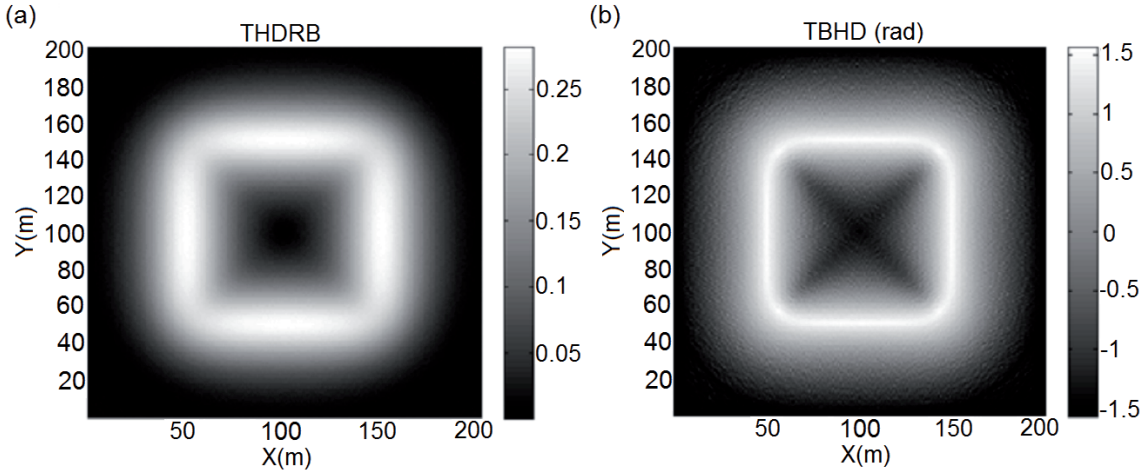

Fig. 8 - Output maps as a result of applying the *THDRB* (a) and *TBHD* (b) filters to the noisy magnetic data in Fig. 7.

4. Improved Euler method (*TBHD*-EUL)

Euler deconvolution (Thompson, 1982; Reid *et al.*, 1990) is a prevalently utilized automatic interpretation technique of potential field data, which employs the genuine anomaly, its derivatives and the given structural index to assess the position parameters of the anomaly source. The accuracy of the evaluated locations depends on the similarity between the defined structural index and the real shape of causative mass (Ravat, 1996; Stavrev, 1997; Barbosa *et al.*, 1999).

The 3D form of the conventional Euler deconvolution equation can be given by (Thompson, 1982; Reid *et al.*, 1990):

$$(x-x_0)\frac{\partial F}{\partial x}+(y-y_0)\frac{\partial F}{\partial y}+(z-z_0)\frac{\partial F}{\partial z}=-N\,(F-B) \tag{5}$$

where F is the potential field data, x, y, and z are the coordinates of the known observational points where the potential field data is measured, x_0, y_0, and z_0 are the unknown source coordinates, B is the background field, and N is the structural index, which describes the nature of the causative source (Reid *et al.*, 1990; Stavrev, 1997).

We have developed the Euler equation using the derivatives of the tilt angle of the *TBHD* to estimate the depth and horizontal location parameters of the sources without requiring the structure index. The 3D Euler deconvolution of the *TBHD* can be expressed in the form:

$$(x-x_0)\frac{\partial TBHD}{\partial x}+(y-y_0)\frac{\partial TBHD}{\partial y}+(z-z_0)\frac{\partial TBHD}{\partial z}=-N\,(TBHD-B) \tag{6}$$

The background field B is assumed as a constant value, so the derivatives of the background are zero. To differentiate Eq. 6 in the x- and y-directions, we can obtain:

$$(x-x_0)\frac{\partial^2 TBHD}{\partial x^2}+(y-y_0)\frac{\partial^2 TBHD}{\partial x\,\partial y}+(z-z_0)\frac{\partial^2 TBHD}{\partial x\,\partial z}+N\,\frac{\partial TBHD}{\partial x}=-\frac{\partial TBHD}{\partial x} \tag{7}$$

$$(x-x_0)\frac{\partial^2 TBHD}{\partial x\,\partial y}+(y-y_0)\frac{\partial^2 TBHD}{\partial y^2}+(z-z_0)\frac{\partial^2 TBHD}{\partial y\,\partial z}+N\,\frac{\partial TBHD}{\partial y}=-\frac{\partial TBHD}{\partial y} \tag{8}$$

Multiplying Eqs. 7 and 8 by $\frac{\partial TBHD}{\partial y}$ and $\frac{\partial TBHD}{\partial x}$, respectively, and subtracting the first from the second, we can get:

$$\begin{aligned}&(x-x_0)\left(\frac{\partial^2 TBHD}{\partial x^2}\cdot\frac{\partial TBHD}{\partial y}-\frac{\partial^2 TBHD}{\partial x\,\partial y}\cdot\frac{\partial TBHD}{\partial x}\right)\\&+(y-y_0)\left(\frac{\partial^2 TBHD}{\partial x\,\partial y}\cdot\frac{\partial TBHD}{\partial y}-\frac{\partial^2 TBHD}{\partial y^2}\cdot\frac{\partial TBHD}{\partial x}\right)\\&+(z-z_0)\left(\frac{\partial^2 TBHD}{\partial x\,\partial z}\cdot\frac{\partial TBHD}{\partial y}-\frac{\partial^2 TBHD}{\partial y\,\partial z}\cdot\frac{\partial TBHD}{\partial x}\right)=0\end{aligned} \tag{9}$$

We define M as $[(\partial TBHD/\partial x)/(\partial TBHD/\partial y)]$ and then calculate the derivatives of M in the x-, y-, and z-directions, we can obtain:

$$\frac{\partial M}{\partial x} = \frac{\partial}{\partial x}\left(\frac{\frac{\partial TBHD}{\partial x}}{\frac{\partial TBHD}{\partial y}}\right) = \frac{\frac{\partial^2 TBHD}{\partial x^2}\cdot\frac{\partial TBHD}{\partial y} - \frac{\partial^2 TBHD}{\partial x\,\partial y}\cdot\frac{\partial TBHD}{\partial x}}{\left(\frac{\partial TBHD}{\partial y}\right)^2} \tag{10}$$

$$\frac{\partial M}{\partial y} = \frac{\partial}{\partial y}\left(\frac{\frac{\partial TBHD}{\partial x}}{\frac{\partial TBHD}{\partial y}}\right) = \frac{\frac{\partial^2 TBHD}{\partial x\,\partial y}\cdot\frac{\partial TBHD}{\partial y} - \frac{\partial^2 TBHD}{\partial y^2}\cdot\frac{\partial TBHD}{\partial x}}{\left(\frac{\partial TBHD}{\partial y}\right)^2} \tag{11}$$

$$\frac{\partial M}{\partial z} = \frac{\partial}{\partial z}\left(\frac{\frac{\partial TBHD}{\partial x}}{\frac{\partial TBHD}{\partial y}}\right) = \frac{\frac{\partial^2 TBHD}{\partial x\,\partial z}\cdot\frac{\partial TBHD}{\partial y} - \frac{\partial^2 TBHD}{\partial y\,\partial z}\cdot\frac{\partial TBHD}{\partial x}}{\left(\frac{\partial TBHD}{\partial y}\right)^2} \tag{12}$$

Rearranging Eqs. 10 to 12 and substituting Eqs. 10 to 12 into Eq. 9, with a factorization we can rewrite:

$$\left(\frac{\partial TBHD}{\partial y}\right)^2\left[(x-x_0)\left(\frac{\partial M}{\partial x}\right)+(y-y_0)\left(\frac{\partial M}{\partial y}\right)+(z-z_0)\left(\frac{\partial M}{\partial z}\right)\right]=0 \quad . \tag{13}$$

Thus

$$(x-x_0)\left(\frac{\partial M}{\partial x}\right)+(y-y_0)\left(\frac{\partial M}{\partial y}\right)+(z-z_0)\left(\frac{\partial M}{\partial z}\right)=0 \quad . \tag{14}$$

We can obtain the location parameters x_0, y_0, and z_0 of the causative mass by working out Eq. 14 based on the *TBHD* filter, since the coordinates of the measurement points, i.e. x, y, and z, are already known.

In applying the *TBHD*-EUL method, to get an accurate depth and horizontal location of the anomaly source, we follow the recommended instructions (clustering methods) by Ma *et al.* (2013), which can be summarized as follows:

1. the distance between the horizontal locations of observed and calculated points is less than half of the window size;
2. applying a small window to remove isolated solutions, assuming that a point belongs to a cluster if the distance between that point and all the other points of the same cluster is smaller than a threshold value not bigger than the size of the window;
3. identifying the fixed solutions by the previous clustering method in more general clusters and achieving a merger of the clusters so that belonging to the same cluster all points whose horizontal centre is less than the maximum horizontal radius of confidence of all the clusters;
4. utilizing a filter that removes the clusters with less than a given number of solutions.

5. *TBHD*-EUL application for synthetic data

We have applied the *TBHD*-EUL method on the gravity and magnetic responses of the above models. Figs. 9 and 10 show the plan and 3D view of the estimated horizontal locations and depths for the buried sources due to the gravity data in Figs. 1 and 3, respectively, using a window size of 9 points (9×9). Fig. 11 shows the histogram of the evaluated depths related to Figs. 9 and 10 after clustering, respectively.

The histograms in Fig. 11 demonstrate two ranges of the different depths related to the two causative sources. The first range of both histograms shows a depth of 3.5 ±5.5 m with two bars indicating a depth of 5.0 ± 0.5 m, close to the true value, representing 81,7 % of the total inferred solutions for free-noise gravity data and 57.1 % for the noise corrupted

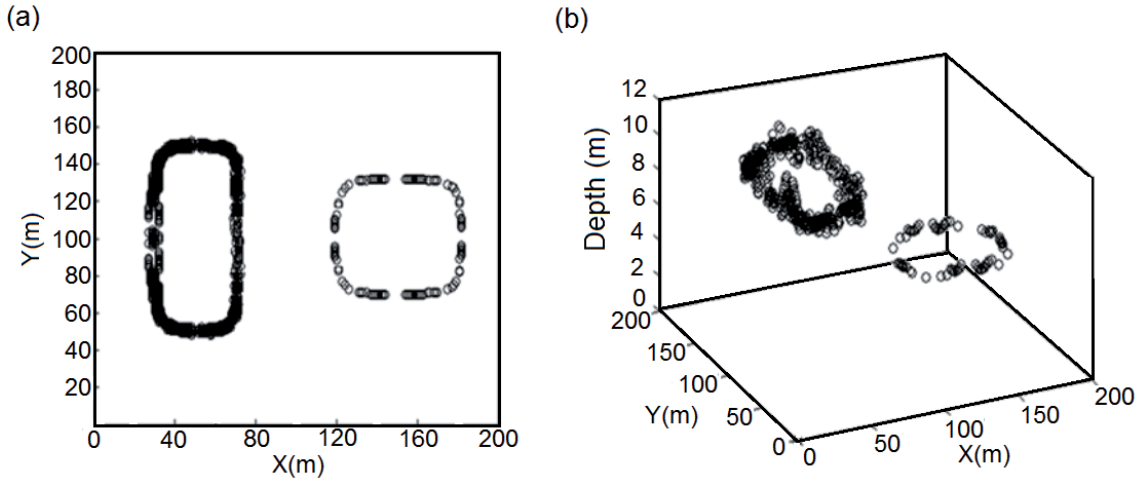

Fig. 9 - Plan and 3D views of the estimated horizontal locations and depths for the buried sources due to the gravity data in Fig. 1.

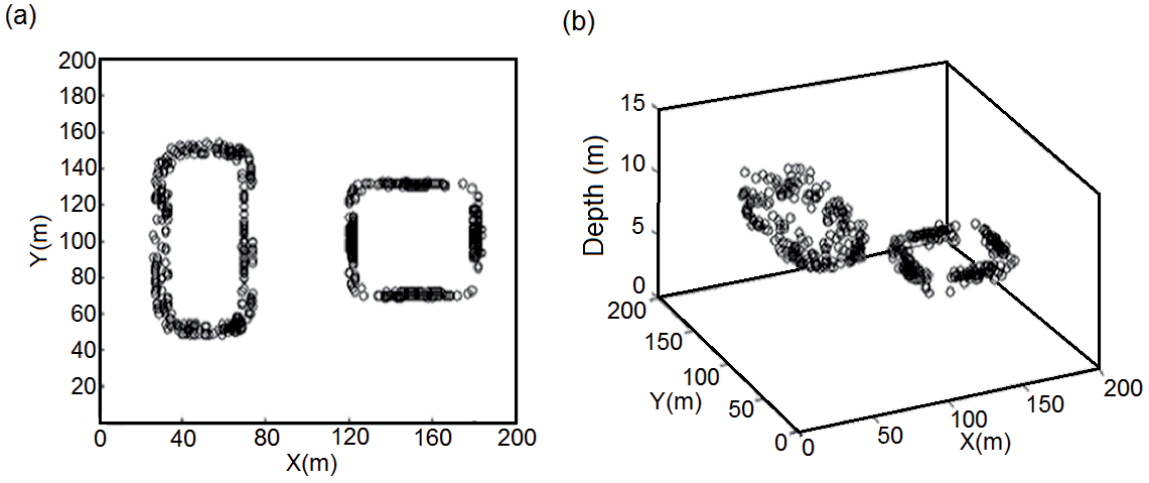

Fig. 10 - Plan and 3D views of the estimated horizontal locations and depths for the buried sources due to the gravity data in Fig. 3.

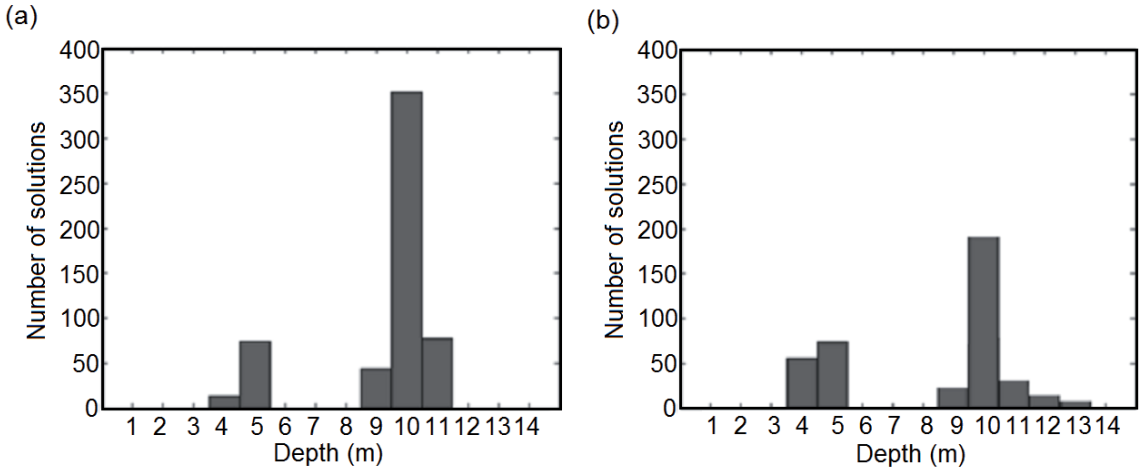

Fig. 11 - The histogram of the evaluated depths related to Figs. 9a and 10b.

gravity data. The second range is a depth of 8.5 to 11.5 m with three bars for the free-noise gravity data as 74.8 % of the estimated Euler depth are between 9.5 to 10.5 m, with an average of 10.3 m and a depth of 8.5 to 13.5 m with five bars for the noise corrupted gravity data as 67.8 % of the estimated depth are between 9.5 to 10.5 m, with an average of 9.65 m.

Depth estimates and computed horizontal locations from the *TBHD*-EUL method for the synthetic magnetic data, with and without random noise, are shown in Figs. 12 and 13, respectively. The evaluated depths are obtained using a moving window size of a 9×9 points over a grid spaced 2×2 m^2. The histogram of the computed depths related to Figs. 12 and 13 after clustering are shown in Fig. 14. According to the histograms, 66.9% of the Euler solutions for free noise magnetic data and 50% of the Euler solutions for the noise corrupted magnetic data are between 19 to 21 m, which is close to the true value, namely 20 m.

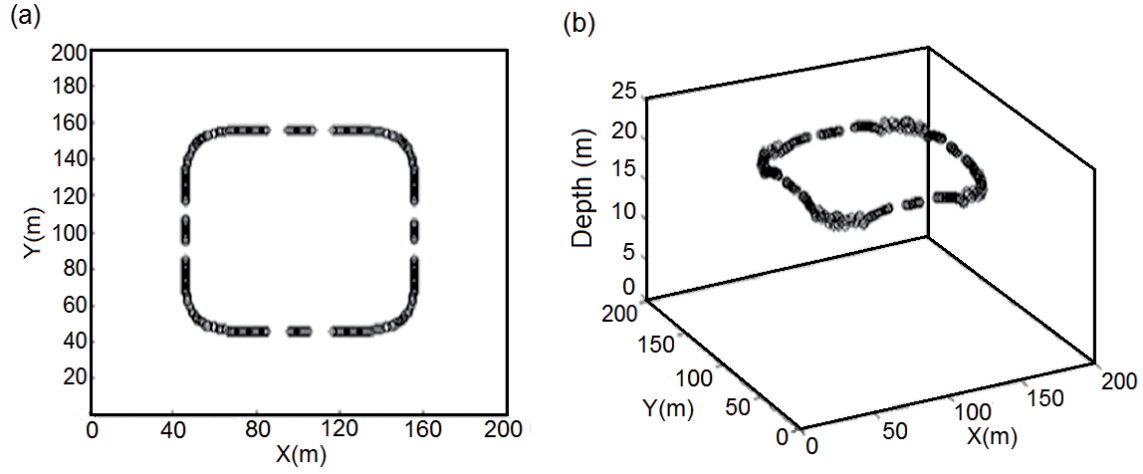

Fig. 12 - Plan and 3D views of the estimated horizontal locations and depths for the buried source due to the magnetic data in Fig. 5.

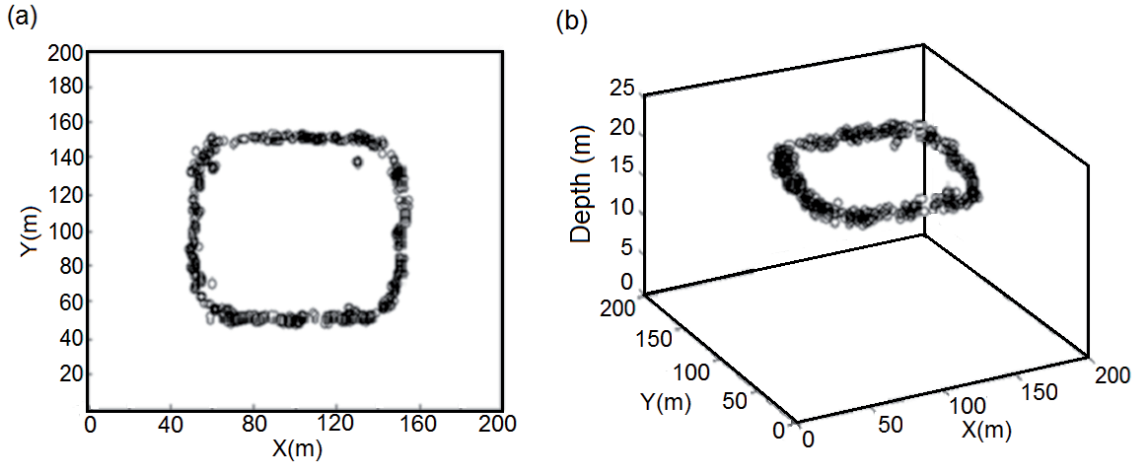

Fig. 13 - Plan and 3D views of the estimated horizontal locations and depths for the buried source due to the magnetic data in Fig. 7.

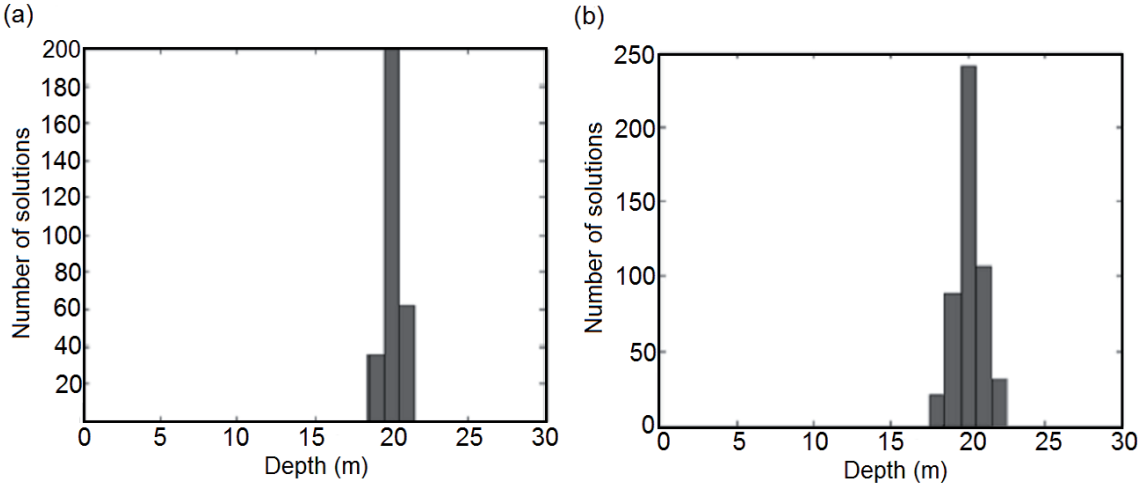

Fig. 14 - The histogram of the evaluated depths related to Figs. 12a and 13b.

6. Real example

The region under study, covering an area about 280 ×130 m^2, is located in the north of Kerman Province, in Iran (Fig. 15). Kerman province can be considered part of the Central Iran Zone in terms of structural units and the extent of sedimentary basins. The Paleozoic to Mesozoic geological formation of the study region consists of dolomite and dolomitic limestone, orbitolina limestone with marl, alternations of marly biomicrite with marl, sandy micrite and siltstone. Quaternary sediments include sand dunes and sheets, silt and clay. Precambrian outcrops comprise volcanic rock, quartzite, sandstone and shale (Fig. 16). The main iron ores in this area are from the oxide group consisting of hematite and magnetite. The aim of the gravity field measurments is underground metal mass detection.

Fig. 15 - Location of the area under study.

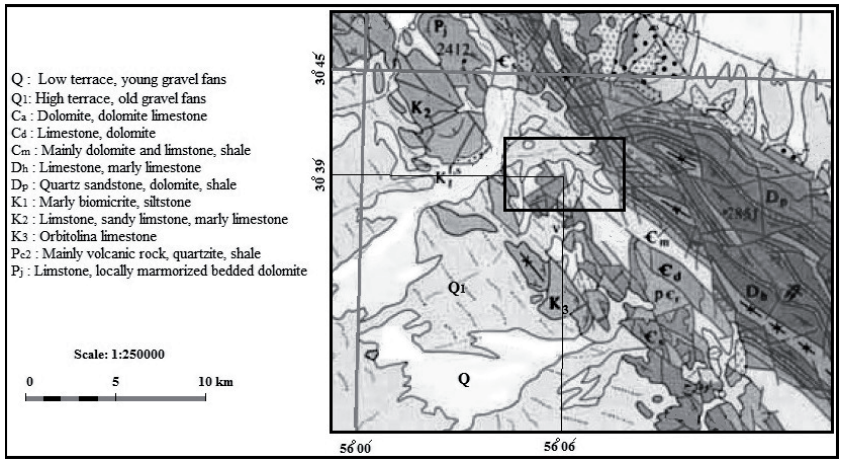

Fig. 16 - Geological map of the region under investigation.

The gravity reading was done with a station spacing of about 3 m, along 45° N-S profiles with a distance of about 6 m. After gravity corrections, the complete Bouguer gravity anomalies map will be obtained, as shown in Fig. 17. As we are looking for the local gravity anomalies, residual gravity anomalies are computed by removing a trend (degree 2) from the Bouguer anomalies. Fig. 18 shows the residual gravity anomalies map of the area under investigation. The positive anomalies over the residual gravity anomalies map are outlined in black, indicating the causative masses with a positive density contrast such as metal deposits.

Fig. 19 shows the *THDRB* and *TBHD* transform of the gravity field data in Fig. 18. The *THDRB* filter (Fig. 19a) shows a very poor performance as the output map is not interpretable. Fig. 19b demonstrates the better continuity of the *TBHD* filter response to the gravity field data in Fig. 18, where the maximum values of the *TBHD* have detected the causative source outline.

Fig. 20 shows the plan and 3D view of the depth estimates obtained by the standard Euler deconvolution method using a window size of 3×3 grid nodes that implies horizontal distances

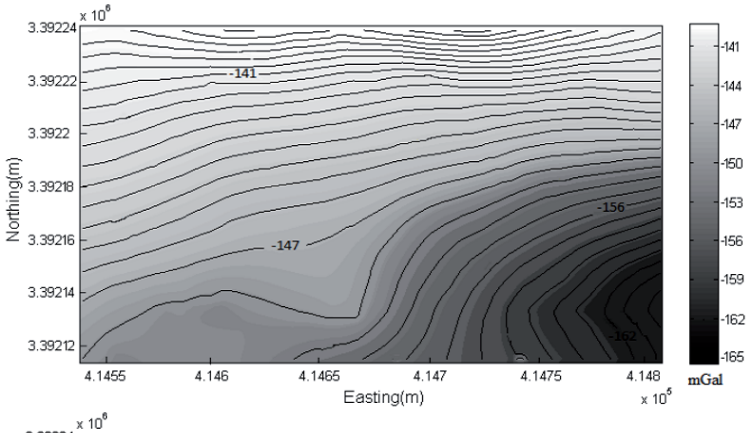

Fig. 17 - The complete Bouguer gravity anomalies map of the area under study.

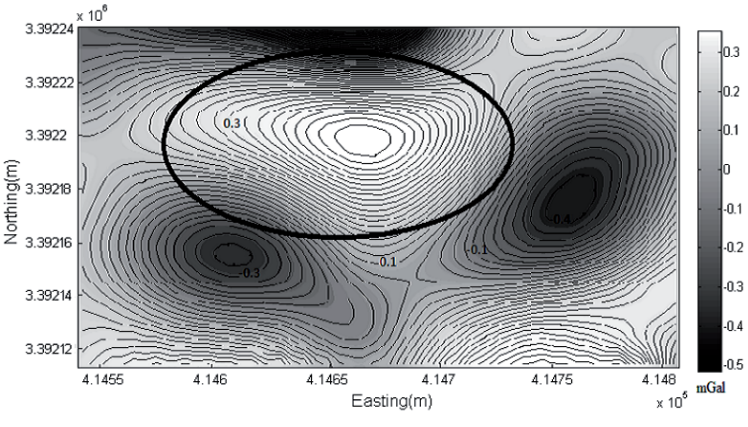

Fig. 18 - Residual gravity anomalies map of the area under investigation.

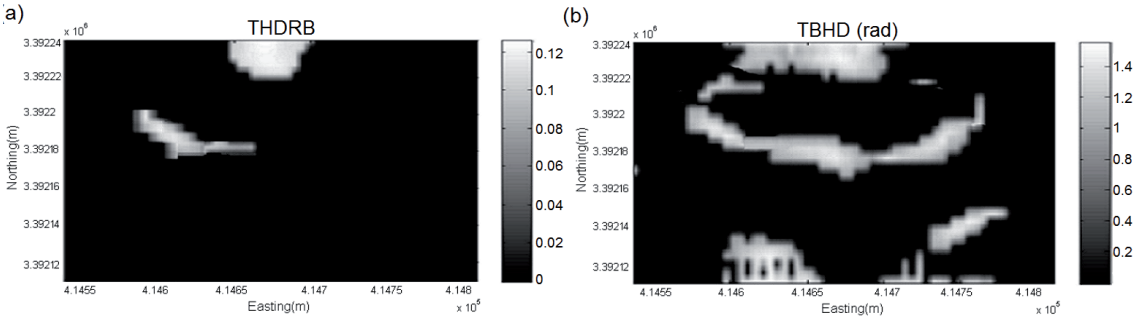

Fig. 19 - The *THDRB* (a) and *TBHD* (b) transform of the gravity field data in Fig. 17.

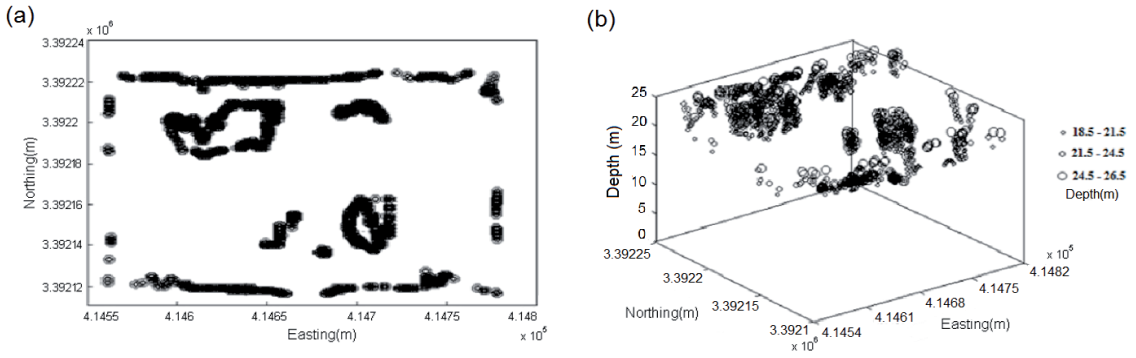

Fig. 20 - Plan and 3D views of the depth estimates obtained by the standard Euler deconvolution method using a window size of 3×3 grid nodes.

approximately $x = 18$ m and $y = 9$ m, with an assumed structural index of 2. The solution positions do not exhibit any distinct boundary for the anomaly source and points are distributed across the map. The histogram in Fig. 22a shows the number of Euler solutions for various depths, where the most of the estimated depth values are in a range from 21.5 to 24.5 m.

Fig. 21 displays the plan and 3D view of the *TBHD*-EUL clustering solutions using a moving window size of 5×5 grid nodes for the gridded *TBHD* data with a constant distance of 5 m. Thus, the horizontal distances in the x and y direction are 25 m. Aggregation of the *TBHD*-EUL solutions coincides approximately with the anomaly source outline, which the *TBHD* transform has depicted in Fig. 19b. Fig. 22b shows the histogram of the depth estimated using the *TBHD*-EUL method. The range of the solutions depth is between 19.5 to 26.5 m where 39.4% of the evaluated depth values indicate a depth of 23 ±0.5 m.

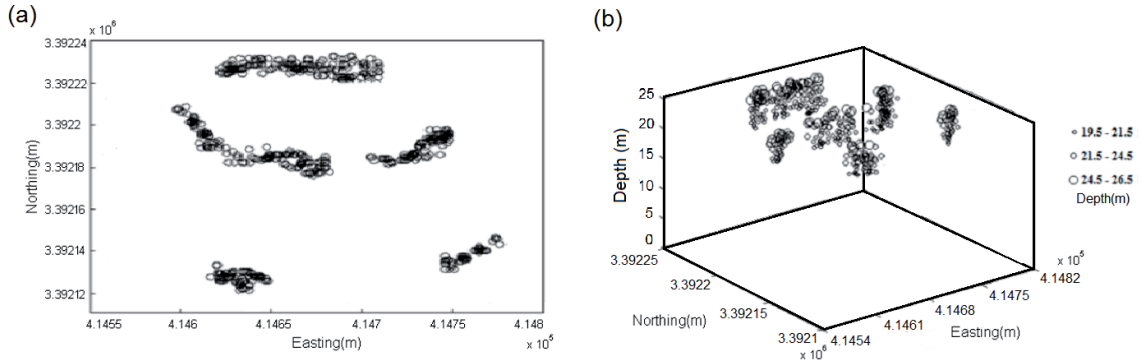

Fig. 21 - Plan and 3D views of the *TBHD*-EUL clustering solutions using a moving window size of 5×5 grid nodes for the gridded *TBHD* data of 5 m.

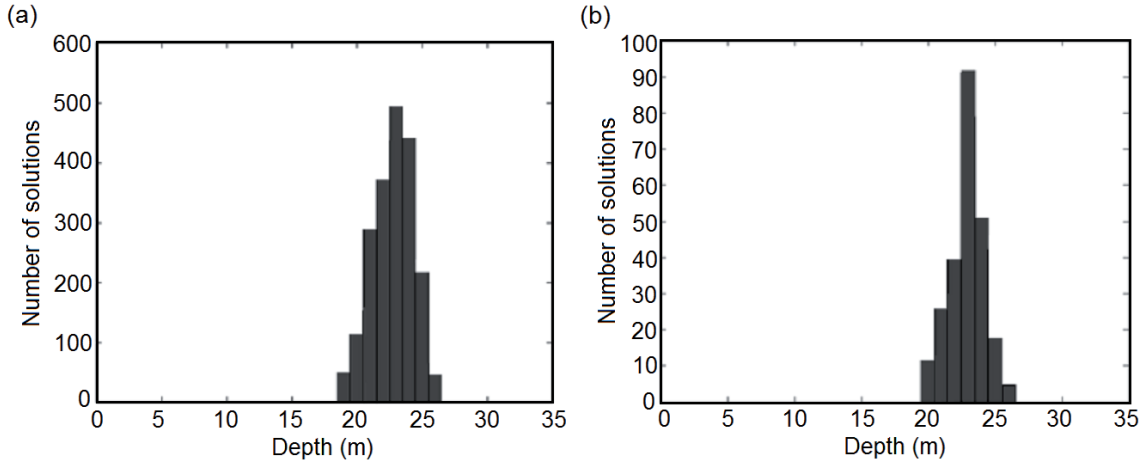

Fig. 22 - Histograms of the depth estimated using the standard Euler deconvolution method (a) and the *TBHD*-EUL method (b).

7. Conclusions

We present two new techniques for the edge and depth determination of potential field causative based on tilt angle of the balanced total horizontal derivative, termed the *TBHD* and *TBHD*-EUL methods. We tested the improved edge-detection method and balanced total horizontal derivative (*THDRB*) filter on the synthetic gravity and magnetic data, with and without added random noise, and real gravity data. The *TBHD* transform results demonstrate a better and more stable performance in delineating the edges of the anomaly mass than the data filtered using the *THDRB* method as the *THDRB* responses show the blurred edges for synthetic models and a unexplainable transformed map for real gravity data. We have also introduced a novel method for estimating the horizontal position and depth of the anomaly causative source, while knowing the structure index is not a requisite, called the *TBHD*-EUL method. The efficiency of the proposed method is illustrated with a set of synthetic gravity and magnetic anomalies, with and without random noise. We also applied the *TBHD*-EUL method to real gravity field data, and compared the inversion results with the standard Euler deconvolution method. In comparison with the Euler deconvolution method, we can see that in the *TBHD*-EUL method the number of calculated points has been reduced, owing to using the potential field data converted by the *TBHD* filter and clustering technique of the solutions. Moreover, the inversion results demonstrate that the *TBHD*-EUL method can successfully compute the location and depth of the sources where the solutions are concentrated over or near the edge. The accuracy of the evaluated depths is higher than the results estimated by the Euler deconvolution method, and thus a more reliable interpretation of the anomaly source depth is achieved.

References

Abdelrahman E.M.; 1990: *Discussion on "A least-squares approach to depth determination from gravity data" by 0.P. Gupta*. Geophys., **55**, 376-378.

Abdelrahman E.M. and El-Araby T.M.; 1993*: A least-squares minimization approach to depth determination from moving average residual gravity anomalies*. Geophys., **58**, 1779-1784.

Abdelrahman E.M., El-Araby T.M., El-Araby H.M. and Abo-Ezz E.R.; 2001: *A new method for shape and depth determinations from gravity data*. Geophys., **66**, 1774-1780.

Alp H., Albora A.M. and Tur H.; 2011: *A view of tectonic structure and gravity anomalies of Hatay Region southern Turkey using wavelet analysis*. J. Appl. Geophys., **75**, 498-505.

Barbosa V.C.F., Silva J.B.C. and Medeiros W.E.; 1999: *Stability analysis and improvement of structural index estimation in Euler deconvolution.* Geophys., **64**, 48-60, doi:10.1190/1.1444529.

Blakely R.J.; 1995: *Potential theory in gravity and magnetic applications*. Cambridge University Press, Cambridge, United Kingdom, 460 pp.

Blakely R.J. and Simpson R.W.; 1986: *Approximating edges of source bodies from magnetic or gravity anomalies*. Geophys., **51**, 1494-1498.

Cooper G.R.J.; 2009: *Balancing images of potential field data*. Geophys., **74**, L17-L20.

Cooper G.R.J. and Cowan D.R.; 2006: *Enhancing potential field data using filters based on the local phase*. Comput. Geosci., **32**, 1585-1591.

Cooper G.R.J. and Cowan D.R.; 2008: *Edge enhancement of potential-field data using normalized statistics*. Geophys., **73**, H1-H4.

Cooper G.R.J. and Cowan D.R.; 2009: *Terracing potential field data*. Geophys. Prospect., **57**, 1067-1071.

Cordell L.; 1979: *Gravimetric expression of graben faulting in Santa Fe Country and the Espanola Basin, New Mexico, Guidebook to Santa Fe Country*. In: Ingersoll R.V. (ed), New Mexico Geol. Soc. Guidebook, 30th Field Conf., pp. 59-64.

Cordell L. and Grauch V.J.S.; 1985: *Mapping basement magnetization zones from aeromagnetic data in the San Juan Basin. New Mexico*. In: Hinze W.J. (ed), The utility of regional gravity and magnetic anomalies maps, Soc. Explor. Geophys., pp. 181-197, doi:10.1190/1.0931830346.ch16.

Eshaghzadeh A.; 2017: *Depth estimation using the tilt angle of gravity field due to the semi-infinite vertical cylindrical source*. J. Geol. Res., ID 3513272, 7 pp., doi:10.1155/2017/3513272.

Eshaghzadeh A. and Kalantari R.S.; 2017: *Canny edge detection algorithm application for analysis of the potential field map*. Earth Sci. India, **10**, 108-125.

Essa K.S.; 2007: *A simple formula for shape and depth determination from residual gravity anomalies*. Acta Geophys., **55**, 182-190.

Evjen H.M.; 1936: *The place of the vertical gradient in gravitational interpretations*. Geophys., **1**, 127-136.

Fedi M. and Florio G.; 2001: *Detection of potential fields source boundaries by enhanced horizontal derivative method*. Geophys. Prospect., **49**, 40-58.

Ferreira F.J.F., de Souza J., Bongiolo A.B.S. and de Castro L.G.; 2013: *Enhancement of the total horizontal gradient of magnetic anomalies using the tilt angle*. Geophys.,**78**, J33-J41.

FitzGerald D., Reid A. and McInerney P.; 2004: *New discrimination techniques for Euler deconvolution*. Comput. Geosci., **30**, 461-469, doi:10.1016/j.cageo.2004.03.006.

Gerovska D. and Arauzo-Bravo M.J.; 2003: *Automatic interpretation of magnetic data based on Euler deconvolution with unprescribed structural index*. Comput. Geosci., **29**, 949-960, doi:10.1016/S0098-3004(03)00101-8.

Görgün E. and Albora A.M.; 2017: *Seismotectonic investigation of Biga Peninsula in SW Marmara Region using steerable filter technique, potential field data and recent seismicity*. Pure Appl. Geophys., **174**, 1-16.

Hood P.J. and Teskey D.J.; 1989: *Aeromagnetic gradiometer program of the Geological Survey of Canada*. Geophys., **54**, 1012-1022.

Hsu S.K.; 2002: *Imaging magnetic sources using Euler's equation*. Geophys. Prospect., **50**, 15-25, doi:10.1046/j.1365-2478.2001.00282.x.

Ma G.; 2013: *Combination of horizontal gradient ratio and Euler (HGR-EUL) methods for the interpretation of potential field data*. Geophys., **78**, J53-J60.

Ma G.; 2014: *The application of extended Euler deconvolution method in the interpretation of potential field data*. J. Appl. Geophys., **107**, 188-194.

Ma G. and Li L.; 2012: *Edge detection in potential fields with the normalized total horizontal derivative*. Comput. Geosci., **41**, 83-87.

Ma G., Huang D. and Liu C.; 2013: *Application of balanced edge detection filters to estimate the location parameters of the causative sources using potential field data*. J. Appl. Geophys., **99**, 18-23.

Miller H.G. and Singh V.; 1994: *Potential field tilt - a new concept for location of potential field sources*. J. Appl. Geophys., **32**, 213-217.

Mushayandebvu M.F., Driel P., Reid A. and Fairhead J.D.; 2001: *Magnetic source parameters of two-dimensional structures using extended Euler deconvolution*. Geophys., **66**, 814-823, doi:10.1190/1.1444971.

Nabighian M.N., Grauch V.J.S., Hansen R.O., LaFehr T.R., Li Y., Peirce J.W., Phillips J.D. and Ruder M.E.; 2005: *The historical development of the magnetic method in exploration*. Geophys., **70**, 33ND-61ND.

Ravat D.; 1996: *Analysis of the Euler method and its applicability in environmental magnetic investigations*. J. Environ. Eng. Geophys., **1**, 229-238.

Reid A.B., Allsop J.M., Granser H., Millet A.J. and Somerton I.W.; 1990: *Magnetic interpretation in three dimensions using Euler deconvolution*. Geophys., **55**, 80-91.

Roest W.R., Verhoef J. and Pilkington M.; 1992: *Magnetic interpretation using the 3-D analytic signal*. Geophys., **57**, 116-125.

Salem A. and Ravat D.; 2003: *A combined analytic signal and Euler method (AN-EUL) for automatic interpretation of magnetic data*. Geophys., **68**, 1952-1961, doi:10.1190/1.1635049.

Salem A., Ravat D., Smith R. and Ushijima K.; 2005: *Interpretation of magnetic data using an enhanced local wavenumber (ELW) method*. Geophys., **70**, L7-L12, doi:10.1190/1.1884828.

Salem A., Williams S., Fairhead D., Smith R. and Ravat D.; 2008: *Interpretation of magnetic data using tilt-angle derivatives*. Geophys., **73**, L1-L10, doi:10.1190/1.2799992.

Stavrev P.Y.; 1997: *Euler deconvolution using differential similarity transformations of gravity or magnetic anomalies*. Geophys. Prospect., **45**, 207-246.

Thompson D.T.; 1982: *Euldph: a new technique for making computer assisted depth estimates from magnetic data*. Geophys., **47**, 31-37.

Thurston J.B. and Smith R.S.; 1997: *Automatic conversion of magnetic data to depth, dip and susceptibility contrast using the SPI method*. Geophys, **62**, 807-813.

Verduzco B., Fairhead J.D. and Green C.M.; 2004: *New insights into magnetic derivatives for structural mapping*. The Leading Edge, **23**, 116-119.

Wijns C., Perez C. and Kowalczyk P.; 2005: *Theta map: edge detection in magnetic data*. Geophys., **70**, 39-43.

Yuan Y., Danian H., Qinglu Y. and Pengyu L.; 2014: *Edge detection of potential field data with improved structure tensor methods*. J. Appl. Geophys., **108**, 35-42.

Corresponding author: Ata Eshaghzadeh
Institute of Geophysics, University of Tehran
Golesorkhi Avenue, 46617-34543 Chaloos, Iran
Phone: +98 11 5228 6946; e-mail: eshagh@alumni.ut.ac.ir